IEEE Robotics and Automation Letters (RA-L) paper, presented at ICRA 2026, Vienna, Austria. Cite as RA-L paper.

Soft Robotic Delivery of Coiled Anchors for Cardiac Interventions

Leonardo Zamora Yañez[1], Jacob Rogatinsky[1], Dominic Recco[2], Sang-Yoep Lee[1], Grace Matthews[1], Andrew P. Sabelhaus[1], David Hoganson[2], and Tommaso Ranzani[1]

***Abstract*—Trans-catheter cardiac intervention has become an increasingly available option for high-risk patients without the complications of open heart surgery. However, current catheter-based platforms suffer from a lack of dexterity, force application, and compliance required to perform complex intracardiac procedures. An exemplary task that would significantly ease minimally invasive intracardiac procedures is the implantation of anchor coils, which can be used to fix and implant various devices. We introduce a robotic platform capable of delivering anchor coils. We develop a kineto-statics model of the robotic platform and demonstrate low positional error. We leverage the passive compliance and high force output of the actuator in a multi-anchor delivery procedure against a motile *in-vitro* simulator with millimeter level accuracy.**

***Index Terms*—Medical Robots and Systems; Soft Robot Applications**

I. Introduction

WIDESPREAD access to minimally invasive, catheter-based, interventions for heart procedures would allow more patients to receive treatment for cardiac pathophysiology, without the risks associated with open-heart surgery (e.g., higher pain levels, longer hospital stays, and complications associated with cardiopulmonary bypass) [1]–[3]. Conventional catheters, while well suited for specific tasks such as guidance of implantable devices and therapeutic interventions, have limited dexterity and stability, which makes it difficult to perform complex procedures [4].

An example of a challenging task with conventional catheters is coiled anchor implantation, which requires newton level contact forces for tissue puncture and stable torque transmission despite remote operation and a dynamic cardiac workspace [5], [6]. Coils can be used to implant pacemaker leads under x-ray fluoroscopy but the implantation process can range from 25 min to several hours with a significant portion of the time spent locating the implantation site [7], [8]. Multiple coils can be implanted to place annuloplasty bands as a treatment for valve regurgitation [9]. Valve regurgitation is a common valve pathology where leaflet coaptation is insufficient to prevent backflow during the cardiac cycle [10]. Tricuspid valve regurgitation (TR) affects over 70 million people globally, including more than 1.6 million in the US, yet fewer than 10,000 procedures are performed annually [11], [12]. The majority of TR cases are treated via open surgery, but these cases still retain a high mortality rate of 8.1% [13] underscoring the need for new approaches.

Surgical robotic systems have emerged to address complexities in navigating tools to mobile anatomic targets while interacting with local structures with minimal visualization [14], [15]. Robotic systems offer surgeons enhanced dexterity compared to traditional low DoF catheters while also enabling feedback to counter the indirect visualization experienced in minimally-invasive surgery [6], [16]. Most existing robotic platforms for minimally invasive cardiac procedures focus on navigation and positioning for ablation and cardiac mapping [17], [18]. Few systems have demonstrated complex procedures involving implantation of devices or tissue manipulation [19], [20]. These systems use rigid yet steerable structures to transmit forces which can introduce torsional instabilities, limiting the range of possible procedures and increasing errors in tip positioning [20]–[22]. While the stiff material of these systems can provide newton level forces, they often necessitate complex computational systems to safely establish contact with the motile heart walls [23] Furthermore, their small size limits compatibility with conventional instruments, often necessitating specialized end-effectors for procedures [23] To date, no robotic architecture addresses the task of coiled anchor implantation, highlighting the need for a trans-catheter system that can deliver coils with stable torque transmission and accuracy in a dynamic heart environment.

We identified four key challenges that need to be addressed for successful minimally invasive coil anchor implantation in the beating heart: 1) continuous force transmission to puncture motile tissue, 2) navigation to moving structures, 3) delivery system for stable torque transmission, and 4) accurate anchor implantation. We present a soft robotic platform able to tackle these challenges to perform coiled anchor implantation (Fig. 1). Our results are presented with the following structure. In Section II, we introduce a coil delivery system with a self-release mechanism to implant coiled anchors into *in-vitro* and *ex-vivo* simulators. We couple the anchors to the tip of the robot via a threaded interface which enables tissue puncture and stable torque transmission during deployment. In section III, we develop a kineto-static model of the robotic manipulator's inflation to achieve closed loop control for accurately tracing clinically relevant paths with millimeter-scale precision. In section IV we characterize the anchor delivery system and demonstrate how a combination of passive compliance by the robot and our closed-loop model can be used to accurately implant a series of nine anchors.

Manuscript received: March, 9, 2025; Revised June, 14, 2025; Accepted September, 11, 2025.

This paper was recommended for publication by Editor Yong-Lae Park upon evaluation of the Associate Editor and Reviewers' comments. This work was supported by the National Institute of Biomedical Imaging and Bioengineering of the NIH, Awards R21EB028363 and R01EB035574. The content is solely the responsibility of the authors and does not necessarily represent the official views of the NIH.

[1]L. Zamora Yañez, J. Rogatinsky, S.-Y. Lee, G. Matthews, A. Sabelhaus, and T. Ranzani are with the Department of Mechanical Engineering, Boston University, Boston, MA 02215, USA tranzani@bu.edu

[2]D. Recco and D. Hoganson are with the Department of Cardiac Surgery, Boston Children's Hospital, Boston, MA 02115, USA

Digital Object Identifier (DOI): see top of this page.

©2026 IEEE

IEEE Robotics and Automation Letters (RA-L) paper, presented at ICRA 2026, Vienna, Austria. Cite as RA-L paper.

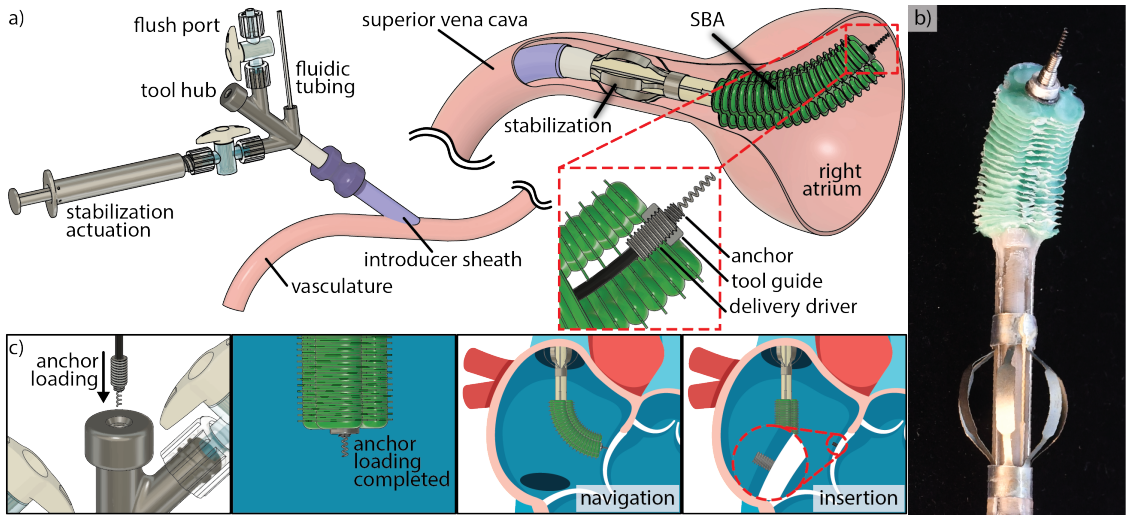

Fig. 1. **Robotic System Overview** (a) Robot overview from the proximal end (left) to the distal end (right). (b) Picture of the prototype with active stabilization and an anchor loaded at the tip. (c) Scheme of loading and deployment of a coiled anchor to the tip of the robot for implantation.

II. Design and Fabrication

A. Robotic System

The robot integrates a soft manipulator based on a Stacked Balloon Actuator (SBA) with a stent-like stabilizer that shifts the fulcrum from the access port to heart-adjacent structures (e.g., superior vena cava, Fig.1(a)) [24], [25]. This architecture improves stability, dexterity, and force transmission for guiding interventional instruments inside the beating heart [26]. The device is capable of radially collapsing from a nominal diameter of 15 mm to 4.5 mm, enabling the robot to navigate through the torturous vasculature for introduction into the heart. Additionally, the robot demonstrated a workspace that fully covers the right atrium, and could exert forces above $0.8\ N$ independent of its configuration for effective tissue interaction [27]. In this work, we focused on the design of the platform for multi-anchor deployment.

The SBA was designed with a central working channel able to accommodate tooling with a diameter of 3.2 mm (9.5 Fr) for anchor delivery (Fig. 1(a)). Three parallel stacks of balloons surround the working channel to enable 3-DoF control required for positioning the anchors. Each stack is composed of twenty balloons with a maximum stroke of 40 mm at 100 kPa, sufficient to reach the His bundle for pacemaker delivery and the tricuspid valve for an annuloplasty. The robot is actuated with saline, a solution of water and table salt, to prevent life threatening air embolisms from forming inside the heart.

Given the displacement of valves during the cardiac cycle, upwards of 10 mm [28], coiled anchors must be securely held at the tip of the robot. To address this challenge, we attached a threaded tool guide to the tip of the SBA for rigid coupling with the anchor delivery driver. The delivery driver holds anchors and mates with the matching threads on the tool guide (Fig. 1(a)). The threaded interface between the tool guide and delivery driver allows for accurate positioning of anchors, while preventing backward sliding of the delivery system when engaging with moving anatomical structures. The interface also enables high force transmission by leveraging SBA inflation to press the coiled end of the anchors against tissue for better capture during implantation.

The central channel terminates in a tool hub where instruments can be inserted through a hemostatic silicone valve (Fig. 1(a)). The fluidic lines, corresponding to each of the three SBA chambers, are connected to three custom syringe pumps. Each syringe pump is driven by a stepper motor controlled by a motor driver (TIC-T825, Pololu). User inputs are received through a keyboard and translated into actuator inputs through a microcontroller (TEENSY40, PJRC) connected to a PC (8NS97AV, HP) via the serial communication ports. The pressure in each chamber was measured using pressure gauges (P-7100-102G-M5, Nidec).

B. Delivery System

To enable anchor implantation, a delivery system with onboard torque sensing was designed (Fig. 2). The system consists of a palm sized handle, a modular driver, and onboard electronics for implantation torque sensing. The delivery system was designed to be operated with a single hand as interventional procedures often require bilateral movement coordination. The handle measures 38 mm in diameter, 150 mm in height, and weighs 70 g.

Although pacemaker electrodes only require one coil for implantation, annuloplasty bands require up to twenty coils for a complete procedure. We address this challenge by designing an anchor delivery module from a braid reinforced catheter (CG412, Terumo Interventional Systems) with a magnetic interface on one end and a threaded driver on the other (Fig. 2(a)). The magnetic interface of the module is designed to allow for fast swapping once a new anchor is ready to be loaded. The catheter was selected due to its high torque transmission while remaining flexible enough to be steered by the robot. The threaded driver features a cylindrical body with external M3$\times$0.5 left-hand threads and internal M2$\times$0.45 right-hand threads. The internal threads couple with the coiled anchors, while the external threads connect the driver-anchor assembly to the SBA via the tool guide.

IEEE Robotics and Automation Letters (RA-L) paper, presented at ICRA 2026, Vienna, Austria. Cite as RA-L paper.

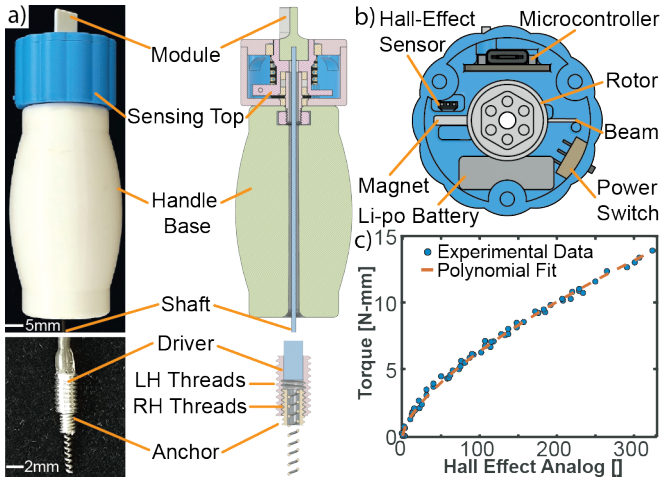

Fig. 2. **Anchor Delivery System** (a) Handle device overview including the replaceable module with a loaded anchor. (b) Electrical components embedded in the handle are used for torque sensing. (c) Numerical model characterizing the magnetic torque sensing system.

The dual-thread driver enables self-release of anchors during deployment (see supplementary video). The self-release mechanism relies on a tissue dependent torque preload between the anchor and the driver. Once the anchor is loaded in the driver, the handle is operated by rotating the shaft counterclockwise, which couples the anchor-driver assembly to the robot via the threaded tool guide. The robot can then press the anchor coil against a surface, with further rotation driving the coil into the medium. Once the coil is fully embedded, the anchor head contacts the medium which increases the torsional resistance of the driver. Further rotation causes the driver-anchor threads to loosen, leading to their automatic decoupling.

Within the handle, the base was designed to rest in the palm of the user as the sensing top was rotated with their index or thumb (see supplementary video). The electronic components fit inside the sensing top of the handle and include a hall effect sensor (DRV5055-Q1, Texas Instruments), a Bluetooth equipped ESP32 microcontroller (Xiao ESP32C3, Seed Studio), and a battery with a power switch (Fig. 2(b)). As torque is transmitted to the handle, an internal flexible beam bends, leading to an angular displacement of the rotor with a neodymium magnet. The rotation forces is measured by a hall effect sensor which in turn increases the signal read by the microcontroller (Fig. 2(b)). The sensor output was calibrated to match the torque experienced by a Force/Torque (F/T) sensor (9105-TW-NANO17-E, ATI) with a resolution of 0.03 N-mm, (Fig. 2(c)). A function mapping sensor signal to torque was derived and transmitted via Bluetooth to a computer for display. The torque was estimated with an average error of 5% and a nominal resolution of 0.07 N-mm.

C. Coiled Anchors

Custom coiled anchors were designed and fabricated (Fig. 3(a)). The size and geometry were based on devices used for pacemaker lead implantation and annuloplasty systems (i.e. 0.7-1.0 mm coil diameter, 6 mm in length) [29], [30]. Each anchor consists of three parts: a threaded head, a sharpened coil, and a pressure fit tube (Fig. 3(b)). The threaded head

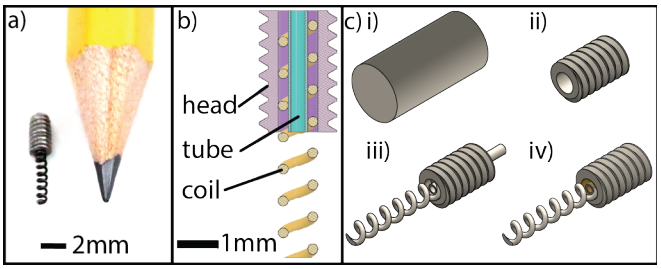

Fig. 3. **Anchor Fabrication** (a) Picture of fabricated anchor. (b) Diagram of anchor components. (c) Anchor fabrication steps.

was fabricated on a lathe (HLV-H, HARDINGE) from 316L stainless steel bar stock (1335T43, McMaster) (Fig. 3(c)-i). The stock material was turned down to 2 mm before threading the exterior surface using an M2×.45 right hand die (a24011700ux0756, uxcell) (Fig. 3(c)-ii). To accommodate the coil, a 1 mm through hole was drilled through the center of the anchor head. The threaded end of the bar stock was then released to produce an anchor head with a diameter of 2 mm, and a length of 3 mm. A single helix coil (2924, Century Spring) was shortened to 8 mm before insertion into the anchor head. A 304 stainless steel tube (5560K653, McMaster), with 0.4 mm diameter, was press fit inside the coil to secure the three part assembly (Fig. 3(c)-iii). The pressed end of the coil was secured with medical adhesive (74795A74, McMaster) and the free end was sharpened using a Dremel (4000-2/30, Dremel) equipped with a grinding wheel (Fig. 3(c)-iv).

III. Modeling and Control

To enable delivery of multiple coils along a trajectory, a requirement in minimally invasive annuloplasty procedures, we developed a path-following algorithm for precise positioning of the robot. We first introduce a mechanics-based model to predict the height of the SBA's chambers under pressure. We then employ a constant curvature framework to derive the kinematics of the robot and incorporate feedback from a 6-DoF sensor as part of a path-following algorithm.

A. Balloon Mechanics Model

The mechanics model predicts the maximum deflection of balloons composed of thin films under pressure. Unlike prior models, which focused on fully inflated balloons or relied on purely geometric estimations [31], [32], our approach is based on Timoshenko's theory for plates to account for large deflections in circular structures [33]. Plate theory describes the maximum deflection w of a circumferentially clamped circular plate, as a function of a pressure p. We define a plate, representative of a balloon half, as having radius $a = 4\ mm$, thickness $h = 0.038\ mm$, and Young's Modulus at 50% strain $E = 13.4\ Nmm^{-2}$ (Fig. 4(a)). In Timoshenko plate theory, h is assumed to be much smaller than w when $\frac{h}{w} << 1$. We use $w = 1.5\ mm$ as a minimum deflection required for each balloon (total SBA stroke of 30 mm) resulting in $\frac{h}{w} = 0.025$. In this case, the strain at the middle of the plate significantly contributes to the overall deflection [34] which leads to:

$$w = 0.662a\sqrt[3]{\frac{pa}{Eh}} \tag{1}$$

IEEE Robotics and Automation Letters (RA-L) paper, presented at ICRA 2026, Vienna, Austria. Cite as RA-L paper.

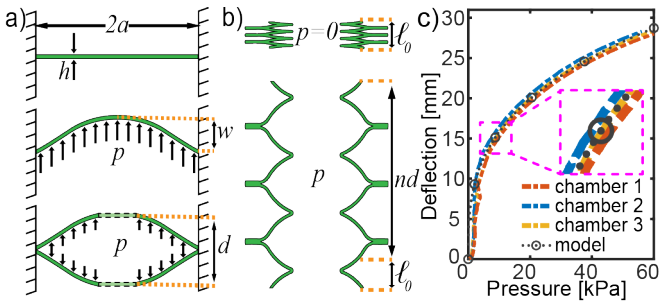

Fig. 4. **Kineto-Static Model** (a) Timoshenko's plate model for large deflection compared to the model for a balloon. (b) Expanded model for a stack of balloons. (c) Comparison of chamber inflation to an analytical model.

To model a balloon composed of two circular plates with open ends, we scaled Eq.(1) by a factor of two to account for the deflection of a second plate. A correction factor $c < 1$ was added to account for the open ends of the actuator balloons, which will decrease the maximum deflection (Fig. 4(b)). The following model describes the maximum deflection d, of the balloon as a function of pressure p, geometric parameters, and physical parameters of the balloon (Fig. 4(a)).

$$d(p) = 1.324ca\sqrt[3]{\frac{pa}{Eh}} \tag{2}$$

The SBA consists of three parallel arrays of vertically stacked balloons. A function, $f(p)$ for the chamber length ℓ, of n stacked balloons due to an internal pressure p, can be defined as a combination of the deflated stack length ℓ_0 and the deflection of the inflated balloons $nd(p)$. In this case, $d(p)$ is the deflection of an inflated balloon as defined in Eq. 2.

$$\ell(p) = nd(p) + \ell_0 \tag{3}$$

We verify Eq.(3), by attaching a 6-DOF electromagnetic (EM) tracker (10006091 Aurora, NDI) to the tip of the SBA during inflation. The three SBA chambers were then inflated with saline to a vertical tip deflection of 30 mm while recording the internal chamber pressure and measuring the vertical length with the EM probe. Fig. 4(c) shows a plot of the pressure vs deflection of each chamber along with the analytical model. The results show a maximum error of 1.34 mm for pressures over 5 kPa which corresponded to a 3.26% error between the analytical model and experimental data. Below 5 kPa (12 mm deflection), the maximum error across all three chambers was found to be 7.82 mm. The larger error at lower pressures can be attributed to the stiction between the films in the balloons, which leads to a lag in inflation. In Fig. (4(c)), the lag manifests as a flattened section where an increase in pressure leads to near zero deflection until the threshold force to separate the layers is reached.

B. Feedback control

To enable navigation inside the heart, we used a kinematic model of the robot based on the constant curvature framework [35]. We define the actuator space parameters as $\boldsymbol{q} = [\ell_1(p_1), \ell_2(p_2), \ell_3(p_3)]$. Where ℓ_i and p_i correspond to the length and pressure of the i^{th} chamber. The parameters arc length s, curvature κ, and angle of the plane containing the arc ϕ, were defined as functions of chamber lengths [36]. Using the relationships for arc angle $\theta = \kappa s$ and arc radius $R = \frac{1}{\kappa}$, the tip position vector $\boldsymbol{r} = [R\cos\phi(1-\cos\theta), R\sin\theta(1-\cos\theta), R\sin\theta]$ was found.

A numerical inverse kinematics solver was developed to trace clinically relevant paths along valve anatomy. Clinicians identified 14 to 20 desired anchor locations based on CT scan data which were then connected with a smooth spline function using MATLAB 2023a. The spline function was discretized into a vector of tip positions $\boldsymbol{g} \in \mathbb{R}^{3\times N}$ where N is the number of points in the path. The current robot's tip position, $\boldsymbol{r_t}$ was obtained from the 6-DoF sensor. Next, we defined the tip position error as $\boldsymbol{e} = \boldsymbol{g_i} - \boldsymbol{r_t}$, where $\boldsymbol{g}_i$ is a point along $\boldsymbol{g}$. From previous work, the robot tip position Jacobian with respect to chamber lengths was defined as, $J(\boldsymbol{r}) = \frac{\partial \boldsymbol{r}}{\partial \boldsymbol{q}}$ [36]. We then used the pseudo-inverse Jacobian, $J^\dagger$, to obtain the required change in chamber lengths, $\Delta\boldsymbol{q}$, needed to minimize the error, Eq. (4). The change in chamber lengths was scaled using a small rate value $\alpha < 1$ to reduce instability and maintain smooth actuation.

$$\Delta\boldsymbol{q} = \alpha J(\boldsymbol{r})^\dagger \boldsymbol{e} \tag{4}$$

After the required chamber lengths are found, we used the inverse of the kineto-static model from Eq. 3 to compute the required pressures $\boldsymbol{p} = f^{-1}(\boldsymbol{q})$ to minimize the $\boldsymbol{e_t}$. Once the absolute tip error $||\boldsymbol{e}_t||$ fell below an error threshold, ε, the current goal point, $\boldsymbol{g}_i$ was considered as reached. The goal point index, i, was then increased to update the current goal point along a path, $\boldsymbol{g}_i = \boldsymbol{g}_{i+1}$. This process was repeated until all points along the path have been reached and can be seen in detail in Algorithm 1.

Algorithm 1 Path tracing algorithm

Input: $\boldsymbol{g}, i, \varepsilon$ - path points, point index, error threshold

while $i < length(\boldsymbol{g})$ **do**
  Get current goal point, $\boldsymbol{g}_i = \boldsymbol{g}[i]$
  Get tip position vector, $\boldsymbol{r}_t$
  Get chamber pressures, $\boldsymbol{p}_t$
  Compute chamber lengths, $\boldsymbol{q}_t = f(\boldsymbol{p}_t)$
  Calculate error, $\boldsymbol{e}_t = \boldsymbol{g}_i - \boldsymbol{r}_t$
  if $||\boldsymbol{e}_t|| < \varepsilon$ **then**
    Update path point index, $i = i + 1$
  else
    Compute chamber lengths, $\hat{\boldsymbol{q}}_{t+1} = \boldsymbol{q}_t + \alpha J(\boldsymbol{r})^\dagger \boldsymbol{e}$
    Compute chamber pressures, $\hat{\boldsymbol{p}}_{t+1} = f^{-1}(\boldsymbol{q}_{t+1})$
    Set system pressures, $\hat{\boldsymbol{p}}_{t+1}$
  end if
end while

The pressures generated by the algorithm were used as inputs to a PID controller running on a microcontroller. The PID controller determined the syringe pump motor velocities required to reach the pressure setpoint. Due to the quasi-static nature of the system, the proportional term dominated for a fast response with a smaller integral term to account for the steady state error.

IEEE Robotics and Automation Letters (RA-L) paper, presented at ICRA 2026, Vienna, Austria. Cite as RA-L paper.

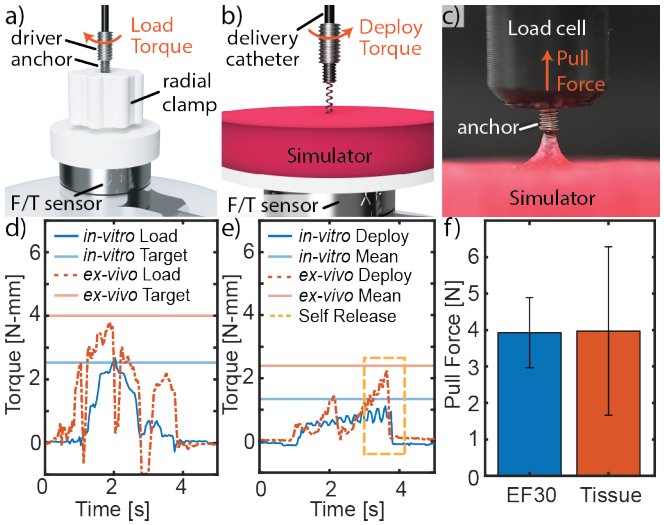

Fig. 5. **Deployment Characterization** (a) Loading radially clamped anchor to threaded driver. (b) Deploying anchor to *in-vitro* simulator using the delivery catheter. (c) Pull force test for an implanted anchor. (d) Anchor loading trial for *in-vitro* and *ex-vivo* simulators. (e) Anchor deployment trial for both simulators with highlighted drop in torque characteristic of the self-release mechanism. (f) Average anchor pull force for *in-vitro* and *ex-vivo* simulators.

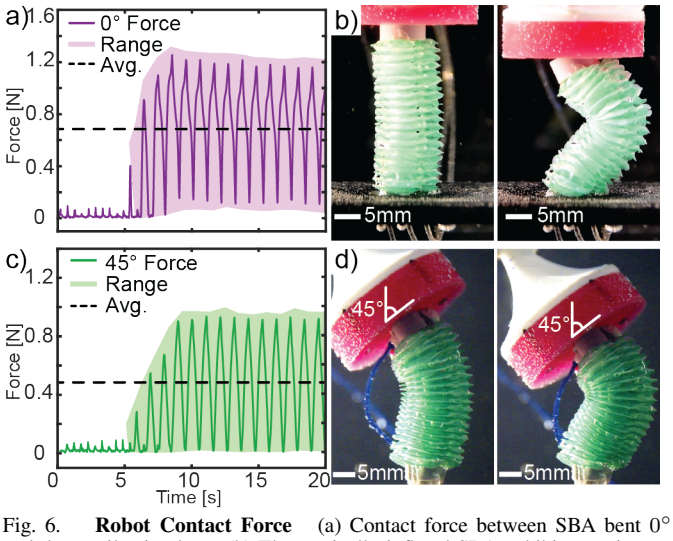

Fig. 6. **Robot Contact Force** (a) Contact force between SBA bent 0° and the motile simulator. (b) The vertically inflated SBA exhibits continuous contact by leveraging its compliant structure. (c) Contact force exerted by a vertically inflated SBA against the moving simulator. (d) At a bending angle of 45°, the SBA can maintain continuous contact while exerting forces at the newton scale.

IV. Results

A. Deployment Characterization

We characterize the anchor implantation process, and the stability of the anchors once implanted in three main steps. First, each anchor is loaded into the driver with predetermined torque values depending on the target medium. Then, the anchor is implanted into a medium to determine the torque required for full deployment. Finally, the implanted anchor is pulled from the medium to measure the failure load.

We validate the ability to implant coils *in-vitro* and *ex-vivo*. The *in-vitro* simulator consists of Ecoflex 00-30 (EF30) silicone (Smooth-On), selected for its comparable properties to porcine heart tissue [37]. The *ex-vivo* simulator utilizes porcine tricuspid valve annulus tissue. Both designs allow for fresh samples to be inserted between trials for consistent testing conditions. Each simulator is mounted to a F/T sensor to verify the loading and deployment torque exerted by the anchor delivery mechanism.

For each simulator, two sets of five anchors were used. Anchor loading began by radially clamping an anchor with a silicone ring to a rigid holder attached to the F/T sensor to measure the torque during loading (Fig. 5(a)). Previous anchor deliveries revealed that insufficient torque preload between the anchor and driver could cause premature release. To prevent this, preload values were selected to ensure full implantation of the coil into the target medium before the self-release mechanism activated. The reverse thread pair in the self-release mechanism inherently limits torque beyond the preload value, embedding a safety threshold into the delivery system. Each anchor was loaded to a target preload torque of 2.5 N-mm for EF30 and 4.0 N-mm for tissue (Fig. 5(d)). Once the anchor reached the desired preload value, the driver-anchor assembly was released and prepared for deployment.

The deployment torque was defined as the maximum torque measured during the anchor implantation process. This value corresponded to the region where the self-release mechanism engaged, leading to slipping between the reverse threads and ultimately anchor release. To obtain this value, the driver-anchor assembly was vertically lowered onto a tissue simulator and fastened to the F/T sensor until 0.5 N of force normal to the surface was measured (Fig. 5(b)). This value was established to ensure consistent puncture of the tissue by the coil required for full implantation. Torque values were recorded throughout deployment and continued until the self-release mechanism was activated to implant the anchor (Fig. 5(e)). The average max deployment torque was found to be 1.23 N-mm for EF30 and 2.55 N-mm for tissue, which demonstrated the effect of a higher preload on the deployment process.

Following deployment, the maximum pull force of each anchor was measured. Each medium with an implanted anchor was mounted to the base of a universal testing machine (5943, Instron) (Fig. 5(c)). The implanted anchor head was then coupled to the load cell using an M2 threaded adapter before raising it at a rate of 0.1 mms^{-1}. The average maximum pull force for EF30 and tissue was 3.94 N and 3.99 N respectively (Fig. 5(f)) which exceeds the 0.52 N required for annuloplasty procedures [38]. The similarity between the pull force for both mediums further supported our use of Ecoflex-30 in our *in-vitro* experiments. The differences in standard deviation between Ecoflex (0.96 N) and tissue (2.3 N) indicate the fibrous nature of tissue adds significant variance to the pull-force tests when compared to a homogeneous medium.

B. Robot Contact with Motile Structures

To deliver anchors, the robot must exert adequate force and maintain constant contact with tissue. We demonstrate how the robot can leverage its inherent softness to passively comply with a moving simulator while exerting the pre-established

IEEE Robotics and Automation Letters (RA-L) paper, presented at ICRA 2026, Vienna, Austria. Cite as RA-L paper.

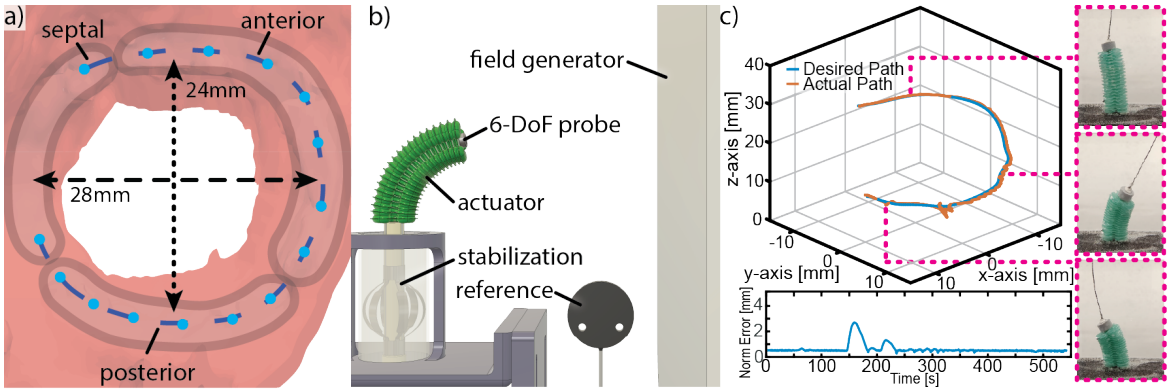

Fig. 7. **Path Tracing** (a) The path of the robot was obtained from a CT scan of the right atrium. The desired implantation locations were selected along the tricuspid valve annulus by a clinician. (b) The device path tracing performance was evaluated underwater using an EM field generator and an EM probe to confirm tip position and error. (c) The target locations were used to generate a smooth path in Euclidean space using spline functions. The tip position of the actuator was measured using an EM tracker.

0.5 N average force for anchor deployment. We chose to mimic the tricuspid valve annulus as the target anatomy due to its high positional variance, making it the most motile valve requiring coil implantation.

An underwater motile simulator was constructed to evaluate the forces exerted on moving samples. The simulator body was fabricated by casting a circular EF30 sample with an 80 mm extrusion to allow for movement underwater without damaging sensing components. The simulator was fastened to the tri-axial F/T sensor and mounted to the end effector of a UR5e Universal Robot Arm. We programmed the arm to cycle 8 mm normal to the simulator's surface to match the upper extent of movement of the tricuspid valve annulus [28]. The frequency was set to 60 beats per minute ($1\ Hz$) to match the heart rate of an adult undergoing cardiac surgery [39]. The simulator and the robotic system were then placed underwater 40 mm apart. The stabilization system was then engaged to secure the base of the actuator against a 35A silicone tube (5236K527, McMaster). The bending angles required to reach the entire tricuspid valve for coil implantation were established by an interventional cardiologist and a CT scan of the right atrium. From the CT scan, we determined that the robot should contact the simulated annulus at angles between 0° (Fig. 6(b)) and 45° (Fig. 6(d)) from the axis normal to the actuator base.

For each angle, five trials were conducted to evaluate the contact force on the motile simulator. Force data was collected for 20 s, and ended after approximately ten cycles of continuous contact with the simulator. Continuous contact was defined as the period in which the SBA exerted a non-zero force on the simulator and was identified by the large amplitude cycles staring at $t = 10s$ in Fig. 6(a,c). The average and maximum forces during continuous contact were measured for both loading conditions. During the vertical loading case, the SBA exerted an average of $0.63\ N$ to the silicone simulator (Fig. 6(a)). For the 45° case, the SBA exerted an average of $0.44\ N$ (Fig. 6(b)). The maximum forces for the 45° and vertical trial were found to be $1.0\ N$ and $1.32\ N$ respectively. The variance of the forces during contact can be attributed to the large displacement of the *in-vitro* simulator. Both maximum forces fall below 5.5 N which is reported as the cutoff for damaging tissue [23] but are greater than the forces used to implant anchors in Section IV.A. These results indicate that the delivery system consistently delivers sufficient force for anchor implantation while remaining within the safe limits for heart tissue contact.

C. Path Tracing

We demonstrate the efficacy of our path-following algorithm by tracing the outline of the tricuspid valve annulus. A labeled CT scan was used to establish 15 anchor implantation locations along the annulus, spaced 5 mm apart (Fig. 7(a)). The path was generated by calculating a series of 3D splines that would sequentially connect all points and the final path was discretized into 500 equally spaced points. The robot was submerged underwater, and the stabilization mechanism was engaged into silicone tubing to brace the base of the actuator (Fig. 7(b)). A 6-DOF EM position sensor (610164, Northern Digital Incorporated) was integrated at the SBA tip to receive position data. The EM field generator was positioned at a clinically relevant distance of 20 cm from the robot, which exceeds the typical distance, 10 cm, from the right atrium to the surface of the chest wall [40].

The path was then used to generate stepper motor commands to move the actuator tip towards the first target point (Fig. 7(c)). After the SBA reached the first point, tip position data was recorded to estimate the error between the actual and desired positions. This process was repeated across the entire path. Along the path, the median error was 0.51 mm with a minimum and maximum error of 0.27 mm and 2.70 mm respectively (Fig. 7(c)).

D. Coiled Anchor Robotic Implantation

To verify the performance of the robot and delivery system, we performed robot-assisted anchor deployment. A series of anchors were deployed into the *in-vitro* motile simulator described in Section IV.B. Each anchor was individually loaded onto the driver using a torque cutoff of 2.5 N-mm. The delivery module was then attached to the delivery handle via the magnetic connecting interface (Fig. 2).

IEEE Robotics and Automation Letters (RA-L) paper, presented at ICRA 2026, Vienna, Austria. Cite as RA-L paper.

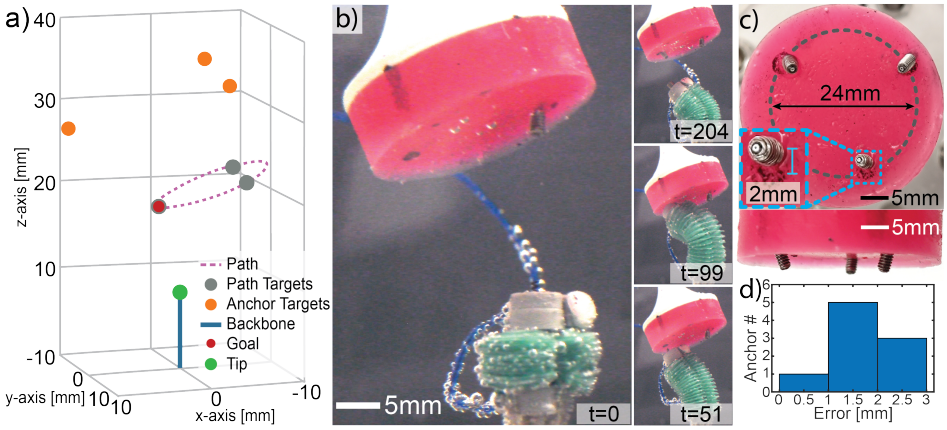

Fig. 8. **Anchor Implantation** (a) User interface displaying the robot backbone, anchor targets on a motile simulator and targets along a circular path. (b) Sequential images of the robot delivering anchors into a motile simulator. At t=0, the robot begins with a loaded anchor. Then the path-planning algorithm is engaged to orient the robot towards the target location. The user then makes the necessary adjustments to contact the motile surface before implantation. Finally, the user rotates the delivery system to implant the anchor. (c) Closeup view of deployed anchors in the *in-vitro* simulator with a side view demonstrating full implantation. (d) Error plot of all nine anchors delivered.

The robot-assisted anchor delivery system was developed in collaboration with clinicians to ensure compatibility with real-world deployment. Typically, a pre-operative CT is obtained to define the anatomy of interest, assess for intra-cardiac anomalies that may impede device implantation, and inform appropriate device sizing. Clinicians used a CT scan of the tricuspid valve to define a desired path along which the device will semi-autonomously navigate (see Section IV.C). We used this path to position the robot prior to anchor implantation.

For this experiment, we focused on defining three annular anchor implantation locations along a circular path with a radius of 24 mm. The three anchor targets were marked onto the *in-vitro* simulator. The simulator and target points were tracked and visualized using an EM tracking system and 6-DoF probe. A user interface was developed to display the anchor targets, robot tip position, and path targets projected from the moving simulator (Fig. 8(a)). The projected path targets served as goal targets to be reached by the close loop path planner prior to contacting the moving in-vitro simulator. Once the close loop controller reached the desired location, the user regained manual control and used the user interface to establish contact with the motile simulator. Once the robot reached the desired anchor target, the driver was rotated to embed the anchor into the simulator. Nine anchors were implanted and their respective errors were measured using image analysis tools (Fig. 8(d)). The final mean error for anchor implantation was 1.82 mm with a minimum and maximum error of 0.86 mm and 2.92 mm, respectively.

V. Conclusions

Coiled anchor implantation is essential for enabling multiple minimally invasive beating heart procedures, with direct relevance to pacemaker lead placement and valve repair. We introduce a soft robotic platform for minimally invasive anchor implantation using a stabilization mechanism to locally brace the base of the robot while leveraging the compliance of the SBA to conform to moving tissue. Our anchor delivery system integrates with standard surgical workflows while overcoming key challenges of device delivery in the beating heart. The delivery system uses a system of threads to rigidly couple the driver to the tip of the robot for high force transmission, precise coil positioning, and to prevent tool slipping. A self-release mechanism allows for full anchor deployment of coils into *in-vitro* and *ex-vivo* simulators without increasing procedural complexity. The threaded coupling provided sufficient force transmission to penetrate tissue, with post-deployment anchor pull forces averaging 3.94 N (*in-vitro*) and 3.99 N (*ex-vivo*), exceeding the forces typically required for valve cinching during an annuloplasty while remaining under the safety threshold for tissue contact.

To support multiple anchor placements, we introduced a path-following algorithm using a kineto-statics model. The model predicts the displacement of a pressurized stack of balloons within 1.34 mm for actuation pressures above 5.0 kPa and enables close-loop control of the robot using a 6-DOF tracker. The system achieved a sub-millimeter tracking error (median error $< 0.52\ mm$) of a path generated from a tricuspid valve CT scan. These results demonstrate how our robotic system can track paths for sequential anchor placements, a key aspect of an annuloplasty, thereby reducing the burden of navigation inside the beating heart.

We demonstrated accurate implantation of coiled anchors on a motile target by combining the delivery mechanism, close-loop controller, and passive compliance of the robot. After coupling the anchor to the robot, the path planning algorithm guided the robot to the target site, with final positioning refined with a user interface and visual confirmation. This approach achieved a 100% success rate implanting nine anchors at 5 mm depth with a mean positioning error of 1.82 mm. From these results we can conclude that this platform can meet the demand for targeting structures such as the His bundle and the tricuspid annulus.

Although the current system lacks force feedback, integrating force sensing and haptic control could be beneficial to the user experience. Future efforts will focus on integration with medical imaging to move towards *in-vivo* validations.

IEEE Robotics and Automation Letters (RA-L) paper, presented at ICRA 2026, Vienna, Austria. Cite as RA-L paper.

REFERENCES

[1] D. L. McDonagh, M. Berger, J. P. Mathew, C. Graffagnino, C. A. Milano, and M. F. Newman, "Neurological complications of cardiac surgery," *The Lancet Neurology*, vol. 13, no. 5, pp. 490–502, 2014.

[2] C. Meduri, J. Chung, J. Gaffney, S. Henley, J. Williams, and H. Gada, "Comparison of us hospital costs between transcatheter aortic valve replacement (tavr) and surgical aortic valve replacement (savr)," *Value in Health*, vol. 20, no. 9, pp. A579–A580, 2017.

[3] H. Sadri, "Breaking down the silos: Transcatheter aortic valve implant versus open heart surgery," in *Healthcare Management Forum*, vol. 33, no. 6. SAGE Publications Sage CA: Los Angeles, CA, 2020, pp. 277–281.

[4] S. Lee, M. Constantinescu, W. Chi, and G. Yang, "Devices for endovascular interventions: technical advances and translational challenges," *NIHR white paper*, 2017.

[5] G. Russo, M. Taramasso, D. Pedicino, M. Gennari, M. Gavazzoni, A. Pozzoli, D. Muraru, L. P. Badano, M. Metra, and F. Maisano, "Challenges and future perspectives of transcatheter tricuspid valve interventions: adopt old strategies or adapt to new opportunities?" *European Journal of Heart Failure*, vol. 24, no. 3, pp. 442–454, 2022.

[6] C. R. Wagner, D. P. Perrin, R. D. Howe, N. Vasilyev, and P. J. D. Nido, "Force feedback in a three-dimensional ultrasound-guided surgical task," *14th Symposium on Haptics Interfaces for Virtual Environment and Teleoperator Systems 2006 - Proceedings*, vol. 2006, pp. 43–48.

[7] A. J. Greenspon, J. D. Patel, E. Lau, J. A. Ochoa, D. R. Frisch, R. T. Ho, B. B. Pavri, and S. M. Kurtz, "Trends in permanent pacemaker implantation in the united states from 1993 to 2009: increasing complexity of patients and procedures," *Journal of the American College of Cardiology*, vol. 60, no. 16, pp. 1540–1545, 2012.

[8] K. P. Jackson, D. D. Hegland, C. FRAZIER-MILLS, J. P. Piccini, J. I. Koontz, B. D. Atwater, J. P. Daubert, and S. J. Worley, "Impact of using a telescoping-support catheter system for left ventricular lead placement on implant success and procedure time of cardiac resynchronization therapy," *Pacing and clinical electrophysiology*, vol. 36, no. 5, pp. 553–558, 2013.

[9] M. Arnold, J. Haug, and M. Landendinger, "Tricuspid annuloplasty: Transcatheter approaches," *Current Cardiology Reports*, vol. 23, 2021.

[10] R. T. Hahn, M. K. Lawlor, C. J. Davidson, V. Badhwar, A. Sannino, E. Spitzer, P. Lurz, B. R. Lindman, Y. Topilsky, S. J. Baron, *et al.*, "Tricuspid valve academic research consortium definitions for tricuspid regurgitation and trial endpoints," *European heart journal*, vol. 44, no. 43, pp. 4508–4532, 2023.

[11] O. Stuge and J. Liddicoat, "Emerging opportunities for cardiac surgeons within structural heart disease," *The Journal of thoracic and cardiovascular surgery*, vol. 132, no. 6, pp. 1258–1261, 2006.

[12] D. Messika-Zeitoun, P. Verta, J. Gregson, S. J. Pocock, I. Boero, T. E. Feldman, W. T. Abraham, J. Lindenfeld, J. Bax, M. Leon, *et al.*, "Impact of tricuspid regurgitation on survival in patients with heart failure: a large electronic health record patient-level database analysis," *European Journal of Heart Failure*, vol. 22, no. 10, pp. 1803–1813, 2020.

[13] F. Alqahtani, C. O. Berzingi, S. Aljohani, M. Hijazi, A. Al-Hallak, and M. Alkhouli, "Contemporary trends in the use and outcomes of surgical treatment of tricuspid regurgitation," *Journal of the American Heart Association*, vol. 6, no. 12, p. e007597, 2017.

[14] B. S. Peters, P. R. Armijo, C. Krause, S. A. Choudhury, and D. Oleynikov, "Review of emerging surgical robotic technology," *Surgical endoscopy*, vol. 32, pp. 1636–1655, 2018.

[15] G. Fagogenis, M. Mencattelli, Z. Machaidze, B. Rosa, K. Price, F. Wu, V. Weixler, M. Saeed, J. E. Mayer, and P. E. Dupont, "Autonomous robotic intracardiac catheter navigation using haptic vision," *Science robotics*, vol. 4, no. 29, p. eaaw1977, 2019.

[16] E. S. Gang, B. L. Nguyen, Y. Shachar, L. Farkas, L. Farkas, B. Marx, D. Johnson, M. C. Fishbein, C. Gaudio, and S. J. Kim, "Dynamically shaped magnetic fields: initial animal validation of a new remote electrophysiology catheter guidance and control system," *Circulation. Arrhythmia and electrophysiology*, vol. 4, pp. 770–777, 10 2011.

[17] C. Pappone, G. Vicedomini, F. Manguso, F. Gugliotta, P. Mazzone, S. Gulletta, N. Sora, S. Sala, A. Marzi, G. Augello, *et al.*, "Robotic magnetic navigation for atrial fibrillation ablation," *Journal of the American College of Cardiology*, vol. 47, no. 7, pp. 1390–1400, 2006.

[18] L. Cruddas, G. Martin, and C. Riga, "Robotic endovascular surgery: current and future practice," in *Seminars in Vascular Surgery*, vol. 34, no. 4. Elsevier, 2021, pp. 233–240.

[19] Z. Machaidze, M. Mencattelli, G. Arnal, K. Price, F.-Y. Wu, V. Weixler, D. W. Brown, J. E. Mayer Jr, and P. E. Dupont, "Optically-guided instrument for transapical beating-heart delivery of artificial mitral chordae tendineae," *The Journal of thoracic and cardiovascular surgery*, vol. 158, no. 5, pp. 1332–1340, 2019.

[20] A. H. Gosline, N. V. Vasilyev, E. J. Butler, C. Folk, A. Cohen, R. Chen, N. Lang, P. J. Del Nido, and P. E. Dupont, "Percutaneous intracardiac beating-heart surgery using metal mems tissue approximation tools," *The International journal of robotics research*, vol. 31, no. 9, pp. 1081–1093, 2012.

[21] N. V. Vasilyev, A. H. Gosline, E. Butler, N. Lang, P. J. Codd, H. Yamauchi, E. N. Feins, C. R. Folk, A. L. Cohen, R. Chen, D. Zurakowski, P. J. D. Nido, and P. E. Dupont, "Percutaneous steerable robotic tool delivery platform and metal microelectromechanical systems device for tissue manipulation and approximation: Closure of patent foramen ovale in an animal model," *Circulation: Cardiovascular Interventions*, vol. 6, pp. 468–475, 8 2013.

[22] H. B. Gilbert, R. J. Hendrick, and R. J. Webster III, "Elastic stability of concentric tube robots: A stability measure and design test," *IEEE Transactions on Robotics*, vol. 32, no. 1, pp. 20–35, 2015.

[23] S. G. Yuen, N. V. Vasilyev, P. J. Del Nido, and R. D. Howe, "Robotic tissue tracking for beating heart mitral valve surgery," *Medical image analysis*, vol. 17, no. 8, pp. 1236–1242, 2013.

[24] J. Rogatinsky, K. Gomatam, Z. H. Lim, M. Lee, L. Kinnicutt, C. Duriez, P. Thomson, K. McDonald, and T. Ranzani, "A Collapsible Soft Actuator Facilitates Performance in Constrained Environments," *Advanced Intelligent Systems*, p. 2200085, jun 2022.

[25] V. T. Vo, L. Z. Yañez, C. Muter, A. M. Moran, M. Saxena, G. Matthews, and T. Ranzani, "Soft, fiber-reinforced bellow actuators," *IEEE Robotics and Automation Letters*, 2025.

[26] J. Rogatinsky, D. Recco, M. Singh, L. Zamora Yañez, G. Matthews, B. Ayers, E. O'Leary, E. T. Roche, D. Hoganson, and T. Ranzani, "A beating-heart procedure with soft robotic guidance," *Advanced Robotics Research*, vol. 1, no. 1, p. 2400023, 2025.

[27] J. Rogatinsky, D. Recco, J. Feichtmeier, Y. Kang, N. Kneier, P. Hammer, E. O'Leary, D. Mah, D. Hoganson, N. V. Vasilyev, *et al.*, "A multifunctional soft robot for cardiac interventions," *Science Advances*, vol. 9, no. 43, p. eadi5559, 2023.

[28] S. Singh-Gryzbon, A. W. Siefert, E. L. Pierce, and A. P. Yoganathan, "Tricuspid valve annular mechanics: interactions with and implications for transcatheter devices," *Cardiovascular Engineering and Technology*, vol. 10, pp. 193–204, 2019.

[29] X. Zhao, J. F. Wenk, M. Burger, Y. Liu, M. K. Das, W. Combs, L. Ge, J. M. Guccione, and G. S. Kassab, "Simulation of mechanical environment in active lead fixation: Effect of fixation helix size," *Journal of Biomechanical Engineering*, vol. 133, no. 6, p. 061006, 06 2011.

[30] A. Mangieri and A. Latib, "Transcatheter innovations in tricuspid regurgitation: Cardioband," *Progress in Cardiovascular Diseases*, vol. 62, no. 6, pp. 482–485, 2019.

[31] W. H. Paulsen, "What is the shape of a mylar balloon?" *The American mathematical monthly*, vol. 101, no. 10, pp. 953–958, 1994.

[32] H. D. Yang and A. T. Asbeck, "A layered manufacturing approach for soft and soft-rigid hybrid robots," *Soft Robotics*, vol. 7, no. 2, pp. 218–232, 2020.

[33] S. Timoshenko, S. Woinowsky-Krieger, *et al.*, *Theory of plates and shells*. McGraw-hill New York, 1959, vol. 2.

[34] S. Way, "Bending of circular plates with large deflection," *Transactions of the American Society of Mechanical Engineers*, vol. 56, no. 7, pp. 627–633, 1934.

[35] R. J. Webster III and B. A. Jones, "Design and kinematic modeling of constant curvature continuum robots: A review," *The International Journal of Robotics Research*, vol. 29, no. 13, pp. 1661–1683, 2010.

[36] B. A. Jones and I. D. Walker, "Kinematics for multisection continuum robots," *IEEE Transactions on Robotics*, vol. 22, no. 1, pp. 43–55, 2006.

[37] C.-K. Park and J. Kim, "Development of a three-dimensional-printed heart model replicating the elasticity, tear resistance, and hardness of pig heart using agilus and tango," *Journal of Mechanics in Medicine and Biology*, vol. 22, no. 03, p. 2240007, 2022.

[38] A. Adkins, J. Aleman, L. Boies, E. Sako, and S. Bhattacharya, "Force required to cinch the tricuspid annulus: an ex-vivo study," *The Journal of heart valve disease*, vol. 24, no. 5, p. 644, 2015.

[39] C. Luo, Z. Duan, Z. Xia, Q. Li, B. Wang, T. Zheng, D. Wang, and D. Han, "Minimum heart rate and mortality after cardiac surgery: retrospective analysis of the multi-parameter intelligent monitoring in intensive care (mimic-iii) database," *Scientific Reports*, vol. 13, no. 1, p. 2597, 2023.

[40] R. Seth, P. Magner, F. Matzinger, and C. Van Walraven, "How far is the sternal angle from the mid-right atrium?" *Journal of general internal medicine*, vol. 17, no. 11, pp. 861–865, 2002.